

Self-Supervised Learning with Noisy Dataset for Rydberg Microwave Sensors Denoising

Zongkai Liu^{1,2,*,§}, Qiming Ren^{1,2,§}, Wenguang Yang^{1,2}, Yanjie Tong^{1,2}, Huiwen Wang^{1,2}, Yijie Zhang^{1,2}, Ruohao Zhi^{1,2}, Junyao Xie^{1,2}, Mingyong Jing^{1,2}, Hao Zhang^{1,2}, Liantuan Xiao^{1,2}, Suotang Jia^{1,2}, Ke Tang³, and Linjie Zhang^{1,2,†}

¹*State Key Laboratory of Quantum Optics Technologies and Devices, Institute of Laser Spectroscopy, Shanxi University, Taiyuan 030006, China*

²*Collaborative Innovation Center of Extreme Optics, Shanxi University, Taiyuan, Shanxi 030006, China. and*

³*Guangdong Provincial Key Laboratory of Brain-inspired Intelligent Computation, Department of Computer Science and Engineering, Southern University of Science and Technology, Shenzhen 518055, China.*

(Dated: January 6, 2026)

We report a self-supervised deep learning framework for Rydberg sensors that enables single-shot noise suppression matching the accuracy of multi-measurement averaging. The framework eliminates the need for clean reference signals (hardly required in quantum sensing) by training on two sets of noisy signals with identical statistical distributions. When evaluated on Rydberg sensing datasets, the framework outperforms wavelet transform and Kalman filtering, achieving a denoising effect equivalent to 10,000-set averaging while reducing computation time by three orders of magnitude. We further validate performance across diverse noise profiles and quantify the complexity-performance trade-off of U-Net and Transformer architectures, providing actionable guidance for optimizing deep learning-based denoising in Rydberg sensor systems.

Keywords: Rydberg atom, Microwave sensor, Self-supervised learning, Denoising.

I. INTRODUCTION

Rydberg atom microwave sensors [1–7] are promising for applied fields such as wideband communications and radar, thanks to their ultra-high microwave electric field sensitivity [8, 9], broad frequency response (DC to THz) [10–12], and International System of Units (SI)-traceable calibration [13–16]. However, their utility in open-environment deployments is limited by noise sources that submerge the signal, such as environmental electromagnetic interference, interatomic interaction noise, and thermal noise [3, 7].

Traditional denoising approaches are ill-suited to this constraint. Multi-measurement averaging suppresses random noise but requires hundreds of repetitions, sacrificing temporal resolution and rendering it incompatible with time-varying signals [17, 18]. Wavelet transform (based on thresholding and signal matching) [19–23] and Kalman filtering (dependent on pre-defined state-space models) [24] perform well for stationary noise but fail to stabilize under the non-stationary noise encountered in real-world Rydberg sensor operation.

Deep learning has emerged as an alternative for adaptive denoising [25]: recurrent neural networks (RNNs) [26–28], long short-term memory (LSTMs) [29, 30] and 1d-convolution neural network model [31–36]

leverage temporal dependencies to separate signals from noise (e.g., in speech processing [37–41]), while Transformers use self-attention to balance noise suppression and signal detail preservation [42–45]. However, a standard deep learning structure (e.g., autoencoders [46–48]) requires paired noisy-clean signal datasets for supervised learning, where clean single-shot signals are experimentally inaccessible for Rydberg sensors. Moreover, theoretically constructed idealized clean data deviate from actual experimental conditions, which readily leads to model overfitting [49, 50].

Here, we develop a self-supervised deep learning framework to Rydberg atom microwave sensors denoising, shown in Fig. 1 (a). It is validated on Rydberg sensing signals in both time and frequency domains and is compared with 10000-set averaging, Kalman filtering and wavelet filtering. It has three key advances for applied use: (1) it enables single-shot denoising with accuracy matching 10,000-set averaging, preserving temporal resolution for dynamic measurements; (2) it eliminates the need for clean reference signals by training on two sets of noisy signals with identical statistical distributions, resolving the labeled data scarcity in quantum sensing; (3) it reduces computation time by three orders of magnitude compared to multi-measurement averaging. Finally, we quantify the complexity-performance trade-off of U-Net and Transformer architectures to guide model selection for specific sensor deployment needs. This work advances the practical utility of Rydberg sensors by bridging deep learning denoising with applied quantum sensing constraints.

* lzk1997@sxu.edu.cn

† zlj@sxu.edu.cn

§ Z.L and Q.R contribute equally to this work.

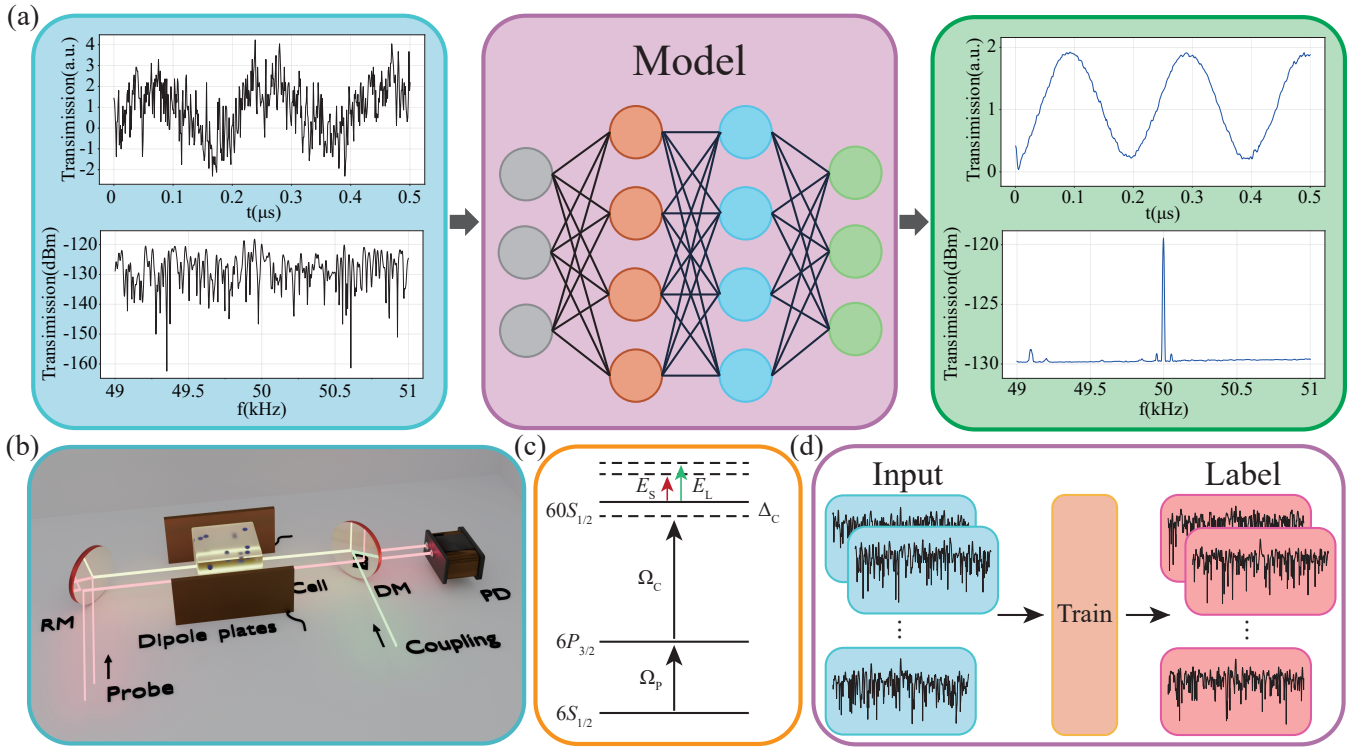


Figure 1. The process of model testing and training. (a) A trained model is capable of generating a clean signal from an input noisy signal including time (upper panel) and frequency domain (lower panel) data. The data are collected from experiment. (b) Experimental setup. The probe light is split into two beams: one counter-propagates with the coupling light inside a cesium vapor cell, while the other outside the cell acts as a reference beam to enable balanced detection. The data set of time domain and frequency domain is collected by an oscilloscope and spectrum analyzer after the balanced detection. The signal electric field E_S and local oscillator electric field E_L interact with the atoms via parallel-plate electrodes. RM-reflect mirror, DM-dichroic mirror, PD-balanced photo-detector. (c) Energy level diagram. The probe light (Rabi frequency Ω_p) and coupling light (Rabi frequency Ω_c , frequency detuning from resonant Δ_c) excite atoms from the ground state $6S_{1/2}$ to the Rydberg state $60S_{1/2}$ via the intermediate state $6P_{3/2}$. The signal and local fields with amplitude E_S and E_L and frequency 63 MHz and 63.05 MHz act on the Rydberg state distribution. (d) During training, the input data and their corresponding labels are independent measurement results of the microwave signal from the same Rydberg atom, differing only in identically independent distributed noise.

II. METHODS

A. Experimental Setup

A Rydberg atom microwave detection system was constructed to acquire noisy intermediate frequency (IF) signals for validating deep learning denoising methods. The experimental setup and energy level diagram are shown in Figs. 1 (b) and (c), respectively. Cesium atoms were confined in a room-temperature glass cell ($5 \times 5 \times 5 \text{ cm}^3$). A 852 nm probe beam (Rabi frequency $\Omega_c/2\pi = 9.06 \text{ MHz}$) excited atoms from $|6S_{1/2}, F = 4\rangle$ to $|6P_{3/2}, F = 5\rangle$, while a 510 nm coupling beam (Rabi frequency $\Omega_c/2\pi = 0.83 \text{ MHz}$) further excited atoms to the $60S_{1/2}$ Rydberg state. The probe beam was split into two: one as a reference outside the cell, and the other counter-propagating with the coupling beam inside to form an electromagnetically induced transparency (EIT) configuration, where the coupling beam modulated

the probe beam's atomic transmission and absorption. The probe beam including the reference are balanced detected by a differential detector (bandwidth 1 MHz and common mode rejection Ratio 40 dB) yielded spectral signals. Both beams' frequencies were stabilized by an ultra-stable cavity (finesse = 2×10^5) and locked to the aforementioned atomic transitions.

The experiment was conducted at room temperature in a microwave anechoic chamber lined with pyramidal foam absorbers, which provides an attenuation of $< 20 \text{ dB}$ for radio frequency (RF) fields at frequency $< 100 \text{ MHz}$ incident normally on the material. Radio frequency (RF) electric field detection adopted an atomic heterodyne scheme: an arbitrary wave generator produced a 63 MHz signal under test (SUT) E_S and a local oscillator (LO) signal E_L frequency detuned from SUT by 50 kHz. These signals were input to parallel brass electrodes (10 cm \times 8 cm in size, 5 cm spacing) to generate a radio frequency (RF) field applied to the atomic system. The atomic energy level is shifted by the SUT and

local fields via the ac Stark shift, which is deduced from the probe transmission [7, 51]. The shift frequency δ is given by $\delta = -\alpha|E_S + E_L|^2/2$, where α is the scalar polarizability. The beating between SUT E_S and local fields E_L generates a 50 kHz IF signal whose amplitude correspond to the SUT's. The probe beam is detected by a balanced differential detector, which converts the light intensity into a voltage signal. This signal is then read out in the time domain using an oscilloscope and in the frequency domain using a spectrum analyzer for deep learning-based denoising. The spectrum analyzer is configured with a resolution bandwidth (RBW) of 10 Hz, 5 averaging cycles for spectrum acquisition, and a frequency sweep range of 49–51 kHz with a step size of 5 Hz. In addition, different intensity of attenuation were applied to the IF signal to simulate open electromagnetic environments, where single-shot signals were submerged in noise but recoverable via multi-measurement averaging.

B. Dataset Design and Training Strategy

The primary goal of training the neural network $f_\theta(\cdot)$ is to learn an optimized weight parameter (θ^*) (encompassing the weights and biases) that minimizes the discrepancy between the network's outputs and the experimental training labels (minimize the loss function $\mathcal{L}(\cdot)$). Mathematically, the training objective is formalized as a constrained minimization problem, and the optimization process is as follows:

$$\theta^* = \arg \min_{\theta} \frac{1}{N} \sum_{i=1}^N \mathcal{L}(f_\theta(x_{\text{train},i}), y_{\text{train},i}), \quad (1)$$

with the size of training dataset N , $x_{\text{train}} = x + n_1$, $y_{\text{train}} = y + n_2$, where x_{train} and y_{train} denote two independent experimental measured data, which consist of ideal clean signals x, y and noise n_1, n_2 drawn from the independent identical noise distribution, i.e., $n_1, n_2 \in \text{Noise}$. The distinction between self-supervised learning and supervised learning lies in their training labels. For supervised learning (e.g., autoencoders [47, 52]), the training label is an ideal, noise-free reference $y_{\text{train}} = y$ (such references are rarely obtainable in sensing scenarios). In contrast, the label used in self-supervised learning (in this work) corresponds to another measurement outcome same condition to training data $y_{\text{train}} = y + n_2$, which eliminates the need for clean reference. The noise n_1, n_2 including environmental electromagnetic interference, interatomic interaction noise, and thermal noise, etc [3]. To adjust the effect of the noise on the signal, we applied an attenuation on the IF signal from the scenario where the IF is above the noise floor to it is submerged by noise but is recognizable after 10000 averaging. After training converges (defined as the training loss remaining stable for 10 consecutive epochs) the optimized weights

θ^* of the deep learning layers are obtained. The prediction process leverages unseen test inputs to output, formulated as

$$\hat{y}_{\text{test}} = f_{\theta^*}(x_{\text{test}}), \quad (2)$$

where x_{test} is independent of x_{train} to ensure unbiased generalization evaluation, the prediction result \hat{y}_{test} is compared to the 10000 set average of the origin data.

Specifically, a Transformer-based end-to-end model was built, along with a dedicated dataset and training protocol, with key details below. In uniform experiments, 10,000 sets of independent and identically distributed (i.i.d.) noisy spectral/time-domain data (1000 consecutive points each set) were collected and partitioned into training, labeling, and testing sets at a 4:4:2 ratio. Specifically, the training set includes measurement result data x_{train} (dimension: 4000, 1000, 1), and independent another set of measurement results y_{train} (dimension: 4000, 1000, 1), while the test set consists of x_{test} (dimension: 2000, 1000, 1). Here $x_{(\cdot)}$ and $y_{(\cdot)}$ denote the training data and their corresponding labels, respectively; the first dimension of the data represents the number of sets, the second dimension denotes the number of consecutive points, and the third dimension is a requirement of the deep learning model. The unlabeled testing data x_{test} was tested against the average of 10,000 original data sets.

Next, to improve the stability of the training and avoid magnitude bias, each data point was standardized: $x' = \frac{x - \mu}{\sigma}$, where x = original data, μ = mean, σ = standard deviation, and x' = standardized data. The data is then fed into a deep learning model for training, whose architecture is shown in Appendix A.

C. Why the Training Process Reduces Noise in Noisy Datasets

To clarify the noise reduction mechanism of the proposed training process, we analyse the optimization of the objective function combined with the statistical properties of noise and the law of large numbers (LLN), as detailed below (adopting MSE loss $\mathcal{L}(a, b) = (a - b)^2$ for simplicity, extendable to other loss functions).

First, we assume that the noise $n_1, n_2 \in \text{Noise}$ satisfies two general properties: (1)Zero mean: $E[n_1] = E[n_2] = 0$ (no systematic bias); (2)Independence on clean signals: $E[x \cdot n_1] = E[y \cdot n_2] = 0$ (noise does not carry signal-related information). The training goal is to minimize the empirical loss:

$$\min_{\theta} J(\theta) = \min_{\theta} \frac{1}{N} \sum_{i=1}^N \mathcal{L}(f_\theta(x_{\text{train},i}), y_{\text{train},i}). \quad (3)$$

Substituting $x_{\text{train},i} = x_i + n_{1,i}$ and $y_{\text{train},i} = y_i + n_{2,i}$, where x_{train} and y_{train} are independent measurement results corresponding to the microwave signal of the same

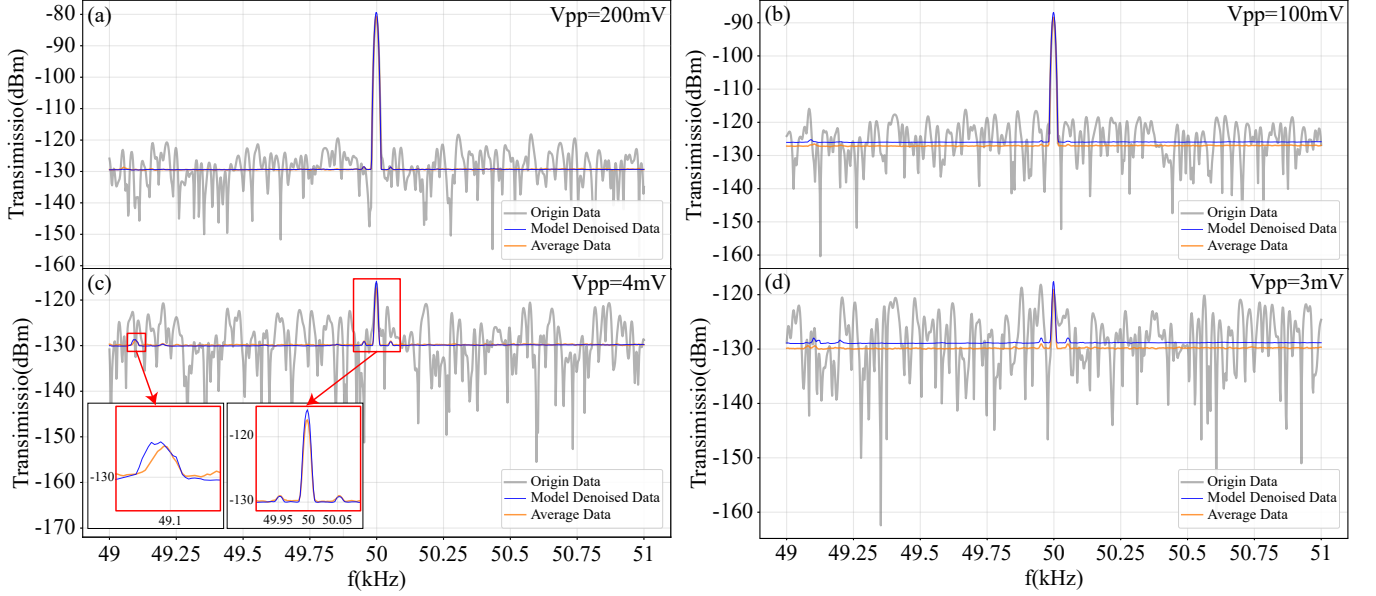


Figure 2. Intermediate frequency (IF) frequency-domain signals under different attenuation levels. IF Signal intensities are labeled in the top-right corner of Subfigures (a)–(d). Gray curves: Single-shot measurements of probe beam transmission signals (attenuating from above noise floor to noise floor level). Green curves: Averaged results of 10,000 measurements (noise-free ground truth, not used in model training), showing noise elimination with only IF signal retained (plus IF sidebands and 49 kHz weak signals under weak attenuation in (c)–(d)). Blue curves: Denoising results of Transformer based model (trained solely on noisy signals), achieving performance comparable to multi-measurement averaging and revealing IF signal, IF sidebands, and 49.1 kHz weak signals. The two red boxes in (c) are zoomed-in views of the averaged and deep learning denoising results at frequencies of 50 kHz and 49.1 kHz, respectively, to illustrate the retained submerged signal.

Rydberg atom differ only in the noise, x and y are clean data. The objective function becomes:

$$J(\theta) = \frac{1}{N} \sum_{i=1}^N [f_\theta(x_i + n_{1,i}) - (y_i + n_{2,i})]^2. \quad (4)$$

For large N , the empirical risk converges to the expected risk by LLN:

$$J(\theta) \xrightarrow{N \rightarrow \infty} \mathbb{E} \left[(f_\theta(x + n_1) - (y + n_2))^2 \right]. \quad (5)$$

Expanding the expectation term and applying the noise assumptions:

$$\mathbb{E} [\dots] = \mathbb{E} \left[(f_\theta(x + n_1) - y)^2 \right] + \sigma_{n2}^2, \quad (6)$$

where the cross term vanishes ($\mathbb{E}[n_2] = 0$ and independence), and $\mathbb{E}[n_2^2] = \sigma_{n2}^2$ (constant noise variance, irrelevant to θ). Since σ_{n2}^2 is fixed, minimizing $J(\theta)$ is equivalent to minimizing the signal fitting error

$$\mathbb{E} \left[(f_\theta(x + n_1) - y)^2 \right]. \quad (7)$$

To achieve this, the model must learn a noise-agnostic mapping, $f_\theta(x + n_1) \rightarrow y$.

Consequently, random fluctuations of n_1 and n_2 are averaged by LLN (for large N), and the model spontaneously suppresses noise by focusing on the clean $x - y$ relationship rather than fitting noise. This explains why the training process reduces noise in noisy datasets.

III. RESULTS

A. Denoising Performance on Frequency-Domain Signals

The deep learning model enables denoising quantum sensing data for both time-domain and frequency-domain signals. Fig. 2 presents its denoising results on IF frequency-domain signals measured by the spectrum analyzer, comparing to the averaged result of 10,000 repeated datasets with i.i.d. noise. From Figs. 2 (a-d), the amplitude of SUT on the electrodes is gradually attenuated from 200 mV to 3 mV, which is used to simulate the scenario where the data is gradually submerged by noise. Since the IF signal arises from the beating of the SUT signal and the local signal, and the frequency of the local signal is adjustable to track the SUT, the frequency of the IF signal is fixed at 50 kHz. Without loss of generality, this configuration can be generalized to SUTs with other frequencies.

For strong-amplitude signals (Figs. 2 (a)–(b)), the model restores noisy data to a level comparable to the 10,000-measurement average, while fully preserving the 50 kHz intermediate frequency (IF) signal. The model outperformed multi-measurement averaging in temporal efficiency: measurement time was reduced by three orders of magnitude (1 hour for 10,000 measurements + averaging vs. 0.7 second for deep learning denoising). For

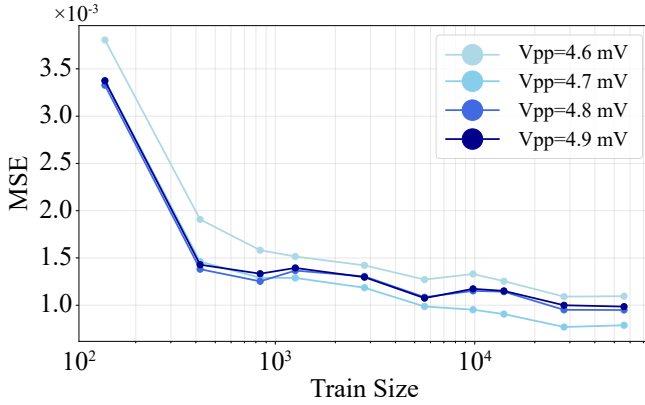


Figure 3. MSE depends on the size of the training dataset in frequency domain. This panel presents the MSE between the denoised results of the deep learning model and the results of 10000-set averaging, under different voltages applied to the dipole plates from 4.6 mV to 4.9 mV. As the training dataset size increases, the MSE decreases.

spectral data with 40 dB attenuation in amplitude (Figs. 2 (c)–(d)), the original signal is completely submerged in noise, however, the model still recovers the IF signal and retains its characteristic components. Notably, non-noise components are retained, as shown in Fig. 2 (c) red box and insets: around the 50 kHz IF signal (two symmetric small peaks) and in the 49 to 49.25 kHz range (small peaks), signals emerge from noise in both the averaged and model denoised results. These are likely characteristic signals, indicating that the model can identify not only post-averaging signals far above the noise floor but also those close to it and submerged by it. The deep learning model successfully recognizes these characteristic signals that are consistent with those of the averaged results. This consistency not only validates the model's ability to capture meaningful patterns, but also confirms that the denoising process is not a spurious artifact of the deep learning framework. In other frequency regions, the denoised results are flatter than the average, showing superior noise suppression in noise-dominated ranges.

Denoising performance was quantified via mean squared error (MSE, against the 10000-measurement average):

$$\text{MSE} = \frac{1}{N} \sum_{i=1}^N (y_i - \bar{y}_i)^2, \quad (8)$$

where N is the number of data points, y_i is the denoised output, and \bar{y}_i is the corresponding 10000-measurement average reference serving as the ground truth. In Fig. 3, the number of training data is varied from 100 to 5×10^4 for peak-to-peak voltage V_{pp} ranging from 4.6 mV to 4.9 mV. After each training process, the MSE is calculated to evaluate how well the denoised results align with the averaging result. It decreases significantly when the number of training data points is over 500, indicating that a moderate increase in training data volume can drasti-

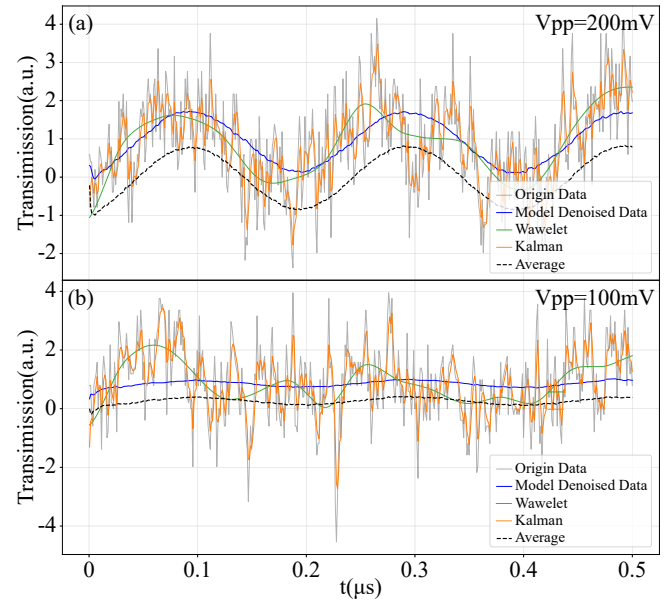


Figure 4. Different denoising models on time-domain signals for $V_{pp}=200$ mV (a) and 100 mV (b). Adopted denoising methods include wavelet denoising (green solid line), Kalman filtering (orange solid line), multi-measurement averaging (black dashed line), and the proposed model's denoising results (blue solid line), all applied to the single-shot measurement result of the probe beam transmission signal (gray solid line). Parameters of wavelet denoising and Kalman filtering were optimized by minimizing the error between their denoising results and the multi-measurement averaging result, as detailed in the main text.

cally boost denoising efficacy, and reaches a plateau as the number of training data points approaches 5×10^4 .

In summary, the model achieves noise suppression performance comparable to that of multi-measurement averaging. It uniquely enables the extraction of noise-submerged signals and the identification of potential characteristic signals from single-shot data.

B. Quantitative Validation of Denoising Performance: Deep Learning vs. Traditional Methods

Fig. 4 validates the proposed deep learning model's superiority over traditional methods (average against 10000 sets, wavelet transform and Kalman filter) in suppressing noise in time series (recorded by the oscilloscope), using IF time-domain signals from Rydberg atom microwave heterodyne detection.

Wavelet transform denoising [22, 53] (green solid line) used coiflets wavelet (4th type) with a threshold of 0.55. Kalman filtering [24] (orange solid line) parameters were set as: process noise variance $Q = 0.0175$ and measurement noise variance $R = 0.06$. To make a fair comparison, the above parameters of traditional methods were optimized by grid search to minimize the MSE between

Table I. MSE for different denoising methods on time domain data for $V_{pp} = 200, 100$ mV cases.

	Deep learning	Kalman filtering	Wavelet
$V_{pp}=200$ mV	$7.71 \times 10^{-4} \pm 1.5 \times 10^{-4}$	$7.0 \times 10^{-2} \pm 1.6 \times 10^{-2}$	$7.1 \times 10^{-2} \pm 2.5 \times 10^{-2}$
$V_{pp}=100$ mV	$7.9 \times 10^{-5} \pm 4.5 \times 10^{-5}$	$1.4 \times 10^{-1} \pm 3.6 \times 10^{-2}$	$2.5 \times 10^{-1} \pm 6.4 \times 10^{-2}$

denoised data by these methods and the averaged result of 10,000 repeated measurements with the same IF signal and i.i.d. noise.

The 10,000-measurement average (black dashed line) was visually smoother than the single-shot result (gray solid line), with noise suppressed and IF signal prominent. The deep learning model’s denoised results (blue solid line) were closer to this average than traditional methods, yielding smoother curves for noisy single-frequency IF signals with three orders of magnitude high temporal efficiency.

For different voltage on the dipole plates, 200 mV, Fig. 4 (a), and 100 mV, Fig. 4 (b), the MSE to averaging result (mean \pm standard deviation from 2000 distinct time-domain signals in the test set) for these three methods is shown in Table I. This two-order-of-magnitude difference in MSE confirms the deep learning model’s significant denoising advantage.

C. Relationship Between Model Complexity and Denoising Performance

To investigate the influence of model complexity on denoising performance, Fig. 5 compares two deep learning architectures (i.e., Transformer- vs. U-net model [54–56], structure diagram shown in Appendix A) on noisy time- and frequency-domain data. The Transformer model (U-net model) has parameter sizes of 4.50×10^5 (1.59×10^4) and training times of 2000 s per epoch (10 s per epoch), respectively; other parameters (e.g., epochs, dataset configuration, and optimizer) were kept consistent.

In both domains, the denoised results of the Transformer-based model are closer to the 10,000-measurement average than those of its counterpart. For the time domain: the alternative architecture fails to capture IF signal features, resulting in outputs that contain significant high-frequency noise alongside the 50 kHz oscillation. In contrast, the Transformer model identifies and extracts the shared IF signal while suppressing noise interference. For the frequency domain: only the IF signal is prominent in the results of the alternative architecture. However, the Transformer model retains the IF signal, its sidebands, and the weak 49.1 kHz signal, showing higher similarity to the 10,000-measurement average. These results demonstrate that increased computational complexity (quantified by training parameters) enhances weak signal extraction, despite longer training times. This enables a more robust recovery of weak signals from noise; future work may adopt deeper or higher-complexity architectures to further enhance performance.

IV. DISCUSSION

In this work, we propose a self-supervised deep learning framework for denoising in Rydberg atom microwave sensors. This framework achieves denoising performance comparable to the averaging method both in the frequency and time domains of microwave sensing signals, while exhibiting extremely low latency. It reduces processing time by three orders of magnitude compared to the averaging method. Compared with Kalman filtering and wavelet transform-based denoising methods, the proposed approach demonstrates a superior denoising effect. Furthermore, by replacing the computational units within the deep learning framework, we identify an optimization direction for further performance enhancement, namely increasing the model’s computational complexity.

The performance of the deep learning denoising framework stems inherently from the model’s ability to learn the intrinsic properties of the target signals [57]. Rydberg atom microwave signals are constrained by the physical laws governing energy level transitions, exhibiting well-defined underlying structures in their amplitude variations, frequency distributions, and temporal evolution. In contrast, environmental interference and quantum fluctuations manifest as random noise components that follow specific statistical laws. By extracting features of common signals from a large dataset, the model can leverage this prior knowledge to retrieve stable shared components from single noisy measurements while suppressing random noise variations across different samples. This process is equivalent to achieving “virtual averaging” in a data-driven manner, preserving the temporal resolution of single-shot measurements without sacrificing the speed limitations associated with traditional averaging methods.

Compared to conventional techniques, the proposed deep learning-based denoising method for quantum sensing offers three distinct advantages. First, the model inference process is extremely fast, with single data processing completed within milliseconds, fully meeting the speed requirements for dynamic process monitoring. Second, centered on data-driven learning, the method eliminates the need for established noise models, enabling stronger adaptability to non-stationary noise commonly encountered in open environments. Third, model training can be accomplished without the need for clean reference signals, making it suited for scenarios in the quantum sensing field where labeled data are scarce.

Future research will focus on the following limitations: for the data-driven paradigm, model performance is highly dependent on the quality of the training data

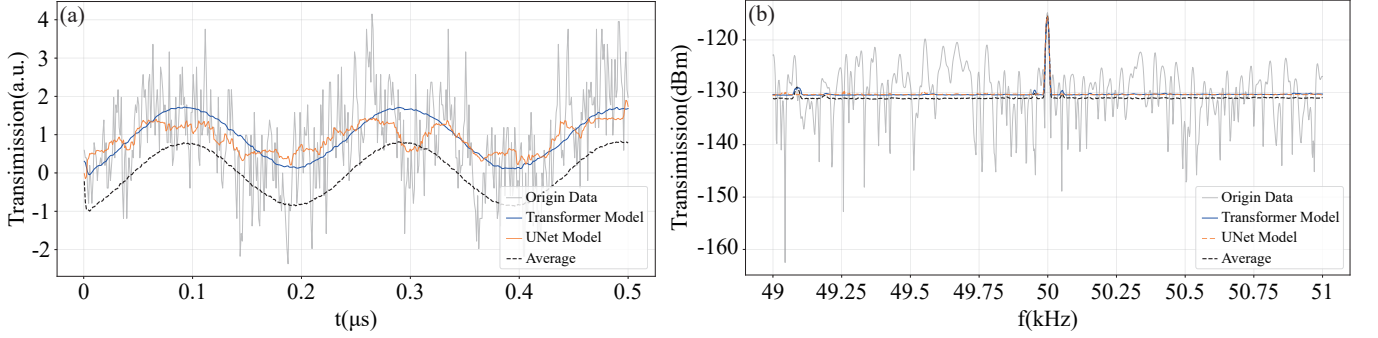


Figure 5. Denoising results of different deep learning models under the same self-supervised architecture. (a) Denoising results of Transformer (blue solid line) and convolution based U-Net structure (orange solid line), both applied to the single-shot measurement result of the probe beam transmission signal (gray solid line); the averaged result of 10,000 measurements (black dashed line) serves as the Ground truth reference. (b) Denoising results of Transformer (blue solid line) and convolution based U-Net structure (orange dashed line) applied to the frequency-domain data of the single-shot measurement result (gray solid line). The Transformer result exhibits not only the intermediate frequency (IF) signal but also its sidebands and the weak 49.1 kHz signal, and is closer to the averaged result than the U-Net.

set, and sufficient data covering various noise scenarios are prerequisite for ensuring denoising effectiveness. Additionally, although the Transformer architecture delivers superior denoising performance, its computational complexity poses challenges for deployment in embedded sensing systems with limited computing resources.

V. ACKNOWLEDGMENT

We acknowledge the the National Key R&D Program of China (grant no. 2022YFA1404003), the National Natural Science Foundation of China (grants T2495252, 12104279, 123B2062, 12574318), Innovation Program for Quantum Science and Technology (Grant No. 2021ZD0302100), the Fund for Shanxi '1331 Project' Key Subjects Construction.

VI. DATA AVAILABILITY

The datasets generated and/or analyzed during the current study are available in the Zenodo repository, accessible via the following Digital Object Identifier (DOI):10.5281/zenodo.18091258

Appendix A: Model structure

The structure of transformer model and U-Net model are shown in Figs. 6 and 7, respectively.

The structure of transformer model is follows. First, a Dense layer projects the demension of data to a 64-dimension space for feature mapping. Second, sine encoding layer (SinePosEncoding) assigns unique vectors via sine values to preserve sequence order. Then, three stacked encoder blocks (each with 8-head multi-head self attention for local-global dependencies, 128-dimension feed-ford neural network with a Gaussian Error Linear Unit (GELU) activation function for signal representation, residual connections for fusion, and dropout (with rate $p = 0.1$)). Finally, a Dense layer maps 64-dimension features back to spectral intensity for denoising. Weights of the above layers were updated via backpropagation by the Adam optimizer (with parameter decay coefficient for first-order momentum $\beta_1 = 0.9$, decay coefficient for second-order momentum $\beta_2 = 0.999$, stability parameter that prevents division by zero $\epsilon = 10^{-7}$, and learning rate 1.0×10^{-5}) with mean square error (MSE) loss (\mathcal{L}) between predictions and y_{train} . The hardware for the deep learning model is a CPU with the parameters: 12th Gen Intel(R) Core(TM) i7-12700 (2.10 GHz).

The U-Net model comprises an encoder, a decoder, and a 1D convolutional layer, where the encoder and decoder are connected via layer concatenation. The encoder consists of three components. The first convolutional layer contains 24 convolution kernels, followed by a LeakyReLU activation function. Subsequently, a max-pooling layer with a pooling size of 2 is applied to halve the temporal resolution. The second convolutional layer further extracts high-level temporal features at the down-sampled temporal scale. The decoder restores temporal resolution using a 1D upsampling layer with a scale factor of 2. Via skip connections, the upsampled features

are concatenated with the corresponding high-resolution features from the encoder, forming the characteristic U-shaped network structure. This design enables the network to effectively fuse low-level temporal detail information and high-level semantic features. Finally, a 1D convolutional layer (with 48 convolution kernels and a kernel size of 3) is used to fuse multi-scale features, accompanied by the LeakyReLU activation function.

[1] Jonathon A Sedlacek, Arne Schwettmann, Harald Kübler, Robert Löw, Tilman Pfau, and James P Shaffer. Microwave electrometry with Rydberg atoms in a vapour cell using bright atomic resonances. *Nat Phys*, 8(11):819–824, 2012.

[2] J. P. Shaffer and H. Kübler. A read-out enhancement for microwave electric field sensing with Rydberg atoms. In Jürgen Stuhler, Andrew J. Shields, and Miles J. Padgett, editors, *Quantum Technol 2018*, volume 10674, page 106740C. International Society for Optics and Photonics, SPIE, 2018.

[3] Mingyong Jing, Ying Hu, Jie Ma, Hao Zhang, Linjie Zhang, Liantuan Xiao, and Suotang Jia. Atomic superheterodyne receiver based on microwave-dressed Rydberg spectroscopy. *Nat Phys*, 16(9):911–915, 2020.

[4] Charles T. Fancher, David R. Scherer, Marc C. St. John, and Bonnie L. Schmittberger Marlow. Rydberg atom electric field sensors for communications and sensing. *IEEE Trans Quantum Eng*, 2:1–13, 2021.

[5] Jinpeng Yuan, Wenguang Yang, Mingyong Jing, Hao Zhang, Yuechun Jiao, Weibin Li, Linjie Zhang, Liantuan Xiao, and Suotang Jia. Quantum sensing of microwave electric fields based on Rydberg atoms. *Rep Prog Phys*, 86(10):106001, 2023.

[6] Bang Liu, Lihua Zhang, Zongkai Liu, Zian Deng, Dongsheng Ding, Baosen Shi, and Guangcan Guo. Electric field measurement and application based on Rydberg atoms. *EMS*, 1(2):1–16, 2023.

[7] Hao Zhang, Yu Ma, Kaiyu Liao, Wenguang Yang, Zongkai Liu, Dongsheng Ding, Hui Yan, Wenhui Li, and Linjie Zhang. Rydberg atom electric field sensing for metrology, communication and hybrid quantum systems. *Science Bulletin*, 69(10):1515–1535, 2024.

[8] Bowen Yang, Yuhang Yan, Xuejie Li, Ling Xiao, Xiaolin Li, L.Q. Chen, Jianliao Deng, and Huadong Cheng. Highly sensitive microwave electrometry with enhanced instantaneous bandwidth. *Phys. Rev. Appl.*, 21:L031003, Mar 2024.

[9] Aojie Zhou, Yi Lin, Ruiqi Mao, Kai Yang, Zhenke Ding, Weipeng Wan, and Yunqi Fu. High-sensitivity Rydberg atom-based field sensing enhancement using miniaturized resonator. *IEEE Trans Antennas Propag*, 73(12):10948–10952, 2025.

[10] David A Anderson and Georg Raithel. Continuous-frequency measurements of high-intensity microwave electric fields with atomic vapor cells. *Appl Phys Lett*, 111(5), 2017.

[11] Charles S Adams, Jonathan D Pritchard, and James P Shaffer. Rydberg atom quantum technologies. *J Phys B: Atom Mol Phys*, 53(1):012002, 2019.

[12] David H Meyer, Zachary A Castillo, Kevin C Cox, and Paul D Kunz. Assessment of Rydberg atoms for wideband electric field sensing. *J Phys B: Atom Mol Phys*, 53(3):034001, jan 2020.

[13] Christopher L. Holloway, Joshua A. Gordon, Steven Jefferts, Andrew Schwarzkopf, David A. Anderson, Stephanie A. Miller, Nithiwadee Thaicharoen, and Georg Raithel. Broadband Rydberg atom-based electric-field probe for SI-traceable, self-calibrated measurements. *IEEE Trans Antennas Propag*, 62(12):6169–6182, 2014.

[14] Christopher L. Holloway, Matthew T. Simons, Joshua A. Gordon, Andrew M. Dienstfrey, David Alexander Anderson, and Georg Raithel. Electric field metrology for SI traceability: Systematic measurement uncertainties in electromagnetically induced transparency in atomic vapor. *J Appl Phys*, 121:233106–233106, 2017.

[15] David Alexander Anderson, Rachel Elizabeth Sapiro, and Georg Raithel. A self-calibrated SI-Traceable Rydberg atom-based radio frequency electric field probe and measurement instrument. *IEEE Trans Antennas Propag*, 69(9):5931–5941, 2021.

[16] Noah Schlossberger, Nikunjkumar Prajapati, Samuel Berweger, Andrew P Rotunno, Alexandra B Artusio-Glimpse, Matthew T Simons, Abrar A Sheikh, Eric B Norrgard, Stephen P Eckel, and Christopher L Holloway. Rydberg states of alkali atoms in atomic vapour as si-traceable field probes and communications receivers. *Nature Reviews Physics*, 6(10):606–620, 2024.

[17] G. Boudreux-Bartels and T. Parks. Time-varying filtering and signal estimation using wigner distribution synthesis techniques. *IEEE Trans on Acoust, Speech, and Signal Process*, 34(3):442–451, 1986.

[18] Marcos Dantus and Vadim V Lozovoy. Experimental coherent laser control of physicochemical processes. *Chemical reviews*, 104(4):1813–1860, 2004.

[19] Quan Pan, Lei Zhang, Guanzhong Dai, and Hongai Zhang. Two denoising methods by wavelet transform. *IEEE Trans Signal Process*, 47(12):3401–3406, 1999.

[20] L. Pasti, B. Walczak, D.L. Massart, and P. Reschiglian. Optimization of signal denoising in discrete wavelet transform. *Chemometr Intell Lab Syst*, 48(1):21–34, 1999.

[21] A. Grossmann and J. Morlet. Decomposition of Hardy functions into square integrable wavelets of constant shape, pages 126–139. Princeton University Press, Princeton, 2006.

[22] CUI Huimin, ZHAO Ruimei, and HOU Yanli. Improved threshold denoising method based on wavelet transform. *Phys Procedia*, 33:1354–1359, 2012. 2012 International Conference on Medical Physics and Biomedical Engineering (ICMPBE2012).

[23] Cigdem Polat Dautov and Mehmet Siraç Özerdem. Wavelet transform and signal denoising using wavelet method. In *2018 26th Signal Processing and Communications Applications Conference (SIU)*, pages 1–4, 2018.

[24] Tamer Basar. *A New Approach to Linear Filtering and Prediction Problems*, pages 167–179. Wiley–Blackwell, 2001.

[25] Siwei Yu, Jianwei Ma, and Wenlong Wang. Deep learning

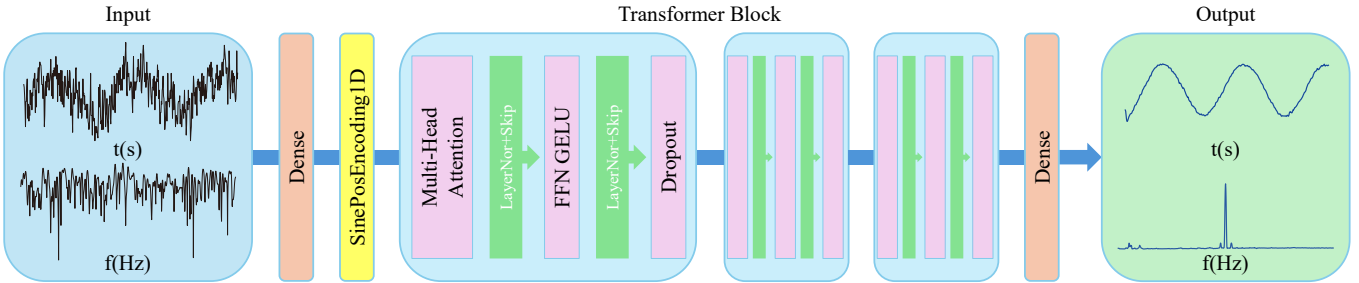


Figure 6. Transformer based mode structure.

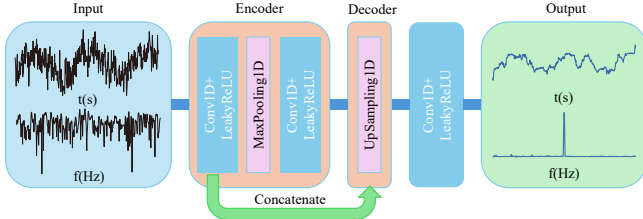


Figure 7. U-Net structure.

for denoising. *Geophys*, 84(6):V333–V350, 2019.

[26] Stephen Grossberg. Recurrent neural networks. *Scholarpedia*, 8(2):1888, 2013.

[27] Dong Eui Caterini, Anthony L. and Chang. *Recurrent Neural Networks*, pages 59–79. Springer International Publishing, Cham, 2018.

[28] Jingyang Wang, Xiaolei Li, Jiazheng Li, QiuHong Sun, and Haiyao Wang. Ngcu: A new rnn model for time-series data prediction. *Big Data Res*, 27:100296, 2022.

[29] Sepp Hochreiter and Jürgen Schmidhuber. Long short-term memory. *Neural Comput*, 9(8):1735–1780, 1997.

[30] Greg Van Houdt, Carlos Mosquera, and Gonzalo Nápoles. A review on the long short-term memory model. *Artif intell rev*, 53(8):5929–5955, 2020.

[31] Zhiqiang Wang, Weizhong Yan, and Tim Oates. Time series classification from scratch with deep neural networks: A strong baseline. In *2017 International Joint Conference on Neural Networks (IJCNN)*, pages 1578–1585, 2017.

[32] Serkan Kiranyaz, Turker Ince, Osama Abdeljaber, Onur Avci, and Moncef Gabbouj. 1-d convolutional neural networks for signal processing applications. In *ICASSP 2019 - 2019 IEEE International Conference on Acoustics, Speech and Signal Processing (ICASSP)*, pages 8360–8364, 2019.

[33] Hassan Ismail Fawaz, Germain Forestier, Jonathan Weber, Lhassane Idoumghar, and Pierre-Alain Muller. Deep learning for time series classification: a review. *Data min knowl disc*, 33(4):917–963, 2019.

[34] Chih-Cheng Chen, Zhen Liu, Guangsong Yang, Chia-Chun Wu, and Qiubo Ye. An improved fault diagnosis using 1D-convolutional neural network model. *Electronics*, 10(1), 2021.

[35] Sana Tonekaboni, Danny Eytan, and Anna Goldenberg. Unsupervised representation learning for time series with temporal neighborhood coding. *arXiv preprint arXiv:2106.00750*, 2021.

[36] Pengfei Zhou, Yunlong Liu, Junli Liang, Qi Song, and Xiangyang Li. Crosslinear: Plug-and-play cross-correlation embedding for time series forecasting with exogenous variables. In *Proceedings of the 31st ACM SIGKDD Conference on Knowledge Discovery and Data Mining V.2, KDD '25*, page 4120–4131, New York, NY, USA, 2025. Association for Computing Machinery.

[37] Alex Graves, Abdel-rahman Mohamed, and Geoffrey Hinton. Speech recognition with deep recurrent neural networks. In *2013 IEEE International Conference on Acoustics, Speech and Signal Processing*, pages 6645–6649, 2013.

[38] Hsün Sak, Andrew Senior, and Françoise Beaufays. Long short-term memory based recurrent neural network architectures for large vocabulary speech recognition. *arXiv preprint arXiv:1402.1128*, 2014.

[39] Felix Weninger, Hakan Erdogan, Shinji Watanabe, Emmanuel Vincent, Jonathan Le Roux, John R Hershey, and Björn Schuller. Speech enhancement with LSTM recurrent neural networks and its application to noise-robust asr. In *International conference on latent variable analysis and signal separation*, pages 91–99. Springer, 2015.

[40] Jane Oruh, Serestina Viriri, and Adekanmi Adegun. Long short-term memory recurrent neural network for automatic speech recognition. *IEEE Access*, 10:30069–30079, 2022.

[41] Jing Wang, Nasir Saleem, and Teddy Surya Gunawan. Towards efficient recurrent architectures: a deep LSTM neural network applied to speech enhancement and recognition. *Cogn Comput*, 16(3):1221–1236, 2024.

[42] Ashish Vaswani, Noam Shazeer, Niki Parmar, Jakob Uszkoreit, Llion Jones, Aidan N Gomez, Łukasz Kaiser, and Illia Polosukhin. Attention is all you need. *Adv Neural Inf Process Syst*, 30, 2017.

[43] Ze Liu, Yutong Lin, Yue Cao, Han Hu, Yixuan Wei, Zheng Zhang, Stephen Lin, and Baining Guo. Swin transformer: Hierarchical vision transformer using shifted windows. In *2021 IEEE/CVF International Conference on Computer Vision (ICCV)*, pages 9992–10002, 2021.

[44] Chi-Mao Fan, Tsung-Jung Liu, and Kuan-Hsien Liu. Sunet: Swin transformer unet for image denoising. In *2022 IEEE International Symposium on Circuits and Systems (ISCAS)*, pages 2333–2337, 2022.

[45] Hongzhou Wang, Jun Lin, Yue Li, Xintong Dong, Xunqian Tong, and Shaoping Lu. Self-supervised pretraining transformer for seismic data denoising. *IEEE Trans Geosci*, 62:1–25, 2024.

[46] Pascal Vincent, Hugo Larochelle, Yoshua Bengio, and

Pierre-Antoine Manzagol. Extracting and composing robust features with denoising autoencoders. In *Proceedings of the 25th International Conference on Machine Learning, ICML '08*, page 1096–1103, New York, NY, USA, 2008. Association for Computing Machinery.

[47] Xugang Lu, Yu Tsao, Shigeki Matsuda, and Chiori Hori. Speech enhancement based on deep denoising autoencoder. In *Interspeech*, 2013.

[48] Dor Bank, Noam Koenigstein, and Raja Giryes. Autoencoders. *Machine learning for data science handbook: data mining and knowledge discovery handbook*, pages 353–374, 2023.

[49] Jake Lever, Martin Krzywinski, and Naomi Altman. Points of significance: model selection and overfitting. *Nat methods*, 13(9):703–705, 2016.

[50] Osval Antonio Montesinos López, Abelardo Montesinos López, and Jose Crossa. Overfitting, model tuning, and evaluation of prediction performance. In *Multivariate statistical machine learning methods for genomic prediction*, pages 109–139. Springer, 2022.

[51] Bang Liu, Li-Hua Zhang, Zong-Kai Liu, Zheng-Yuan Zhang, Zhi-Han Zhu, Wei Gao, Guang-Can Guo, Dong-Sheng Ding, and Bao-Sen Shi. Highly sensitive measurement of a megahertz rf electric field with a rydberg-atom sensor. *Phys Rev Appl*, 18(1):014045, 2022.

[52] Ryandhimas E. Zezario, Tassadaq Hussain, Xugang Lu, Hsin-Min Wang, and Yu Tsao. Self-supervised denoising autoencoder with linear regression decoder for speech enhancement. In *ICASSP 2020 - 2020 IEEE International Conference on Acoustics, Speech and Signal Processing (ICASSP)*, pages 6669–6673, 2020.

[53] Hai-Tao Fang and De-Shuang Huang. Noise reduction in lidar signal based on discrete wavelet transform. *Opt Commun*, 233(1):67–76, 2004.

[54] Olaf Ronneberger, Philipp Fischer, and Thomas Brox. U-net: Convolutional networks for biomedical image segmentation. In *International Conference on Medical image computing and computer-assisted intervention*, pages 234–241. Springer, 2015.

[55] Maximilian P. Reymann, Tobias Würfl, Philipp Ritt, Bernhard Stimpel, Michal Cachovan, A. Hans Vija, and Andreas Maier. U-net for spect image denoising. In *2019 IEEE Nuclear Science Symposium and Medical Imaging Conference (NSS/MIC)*, pages 1–2, 2019.

[56] Nabil Ibtehaz and M. Sohel Rahman. Multiresunet : Rethinking the u-net architecture for multimodal biomedical image segmentation. *Neural Netw*, 121:74–87, 2020.

[57] Saeed Izadi, Darren Sutton, and Ghassan Hamarneh. Image denoising in the deep learning era. *Artif Intell Rev*, 56(7):5929–5974, 2023.